

## Quantum effects in Ar+HF rotationally inelastic scattering: A semiclassical interpretation

James J. C. Barrett, Howard R. Mayne, and Mark Keil

Citation: *The Journal of Chemical Physics* **100**, 304 (1994); doi: 10.1063/1.466999

View online: <http://dx.doi.org/10.1063/1.466999>

View Table of Contents: <http://scitation.aip.org/content/aip/journal/jcp/100/1?ver=pdfcov>

Published by the **AIP Publishing**

---

### Articles you may be interested in

[Rotational relaxation rates in HF and Ar–HF from the direct inversion of pressure broadened linewidths](#)  
J. Chem. Phys. **75**, 4927 (1981); 10.1063/1.441932

[The rotational and hyperfine spectrum of Ar–HF](#)  
J. Chem. Phys. **74**, 6539 (1981); 10.1063/1.441113

[A uniform semiclassical sudden approximation for rotationally inelastic scattering](#)  
J. Chem. Phys. **73**, 1222 (1980); 10.1063/1.440232

[Determination of the structure of ArHF](#)  
J. Chem. Phys. **60**, 3208 (1974); 10.1063/1.1681508

[Semiclassical Transition Probabilities for Rotationally Inelastic Scattering](#)  
J. Chem. Phys. **55**, 510 (1971); 10.1063/1.1675781

---



# Quantum effects in Ar+HF rotationally inelastic scattering: A semiclassical interpretation

James J. C. Barrett and Howard R. Mayne

*Department of Chemistry, University of New Hampshire, Durham, New Hampshire 03824-3598*

Mark Keil

*Department of Physics and Astronomy, University of Oklahoma, Norman, Oklahoma 73019-0225*

(Received 1 June 1993; accepted 15 September 1993)

Invoking a semiclassical approach to state-to-state rotationally inelastic scattering, this study seeks to determine the origin of several novel features observed in earlier quantum mechanical calculations [Rawluk *et al.*, Chem. Phys. Lett. **202**, 291 (1993)]. These features were absent from comparable classical trajectory calculations. The semiclassical (classical path) method used here treats the relative motion of Ar and HF classically, while the HF rotation is treated quantum mechanically by expansion in a rigid rotor basis set. This semiclassical approach reproduces the exact quantum results very well. The time dependence of the classical path allows a detailed study of the role played by the potential energy surface governing the dynamics. In particular, the behavior of the expansion coefficients  $\langle Y_{jm} | \Psi(t) \rangle$  in the complex plane is very revealing. From this analysis, it is clear that the quantum effects stem from a balance between the attractive and repulsive parts of the potential.

## I. INTRODUCTION

Recent experimental<sup>1</sup> and computational<sup>2</sup> studies of rotationally inelastic scattering of HF by Ar show several unexpected and previously unobserved features. These features apparently have a quantum mechanical origin, as illustrated by their complete absence from corresponding classical calculations.<sup>2</sup> The computationally converged state-to-state “exact” quantum differential cross sections (DCS) also show pronounced isotope effects when compared to Ar+DF scattering. The realistic nature of these calculations, carried out on a potential energy surface fitted to spectroscopic precision for the Ar+HF van der Waals molecule,<sup>3</sup> is strongly substantiated by good reproduction of experimental DCS measurements for state-resolved Ar+HF scattering.<sup>2</sup> Despite numerous computational investigations, however, the physical origin of the quantum features was not fully elucidated by our recent study.

Earlier investigations into the origin of quantum features observed for rotationally inelastic scattering focused on systems with no substantial attractive anisotropy<sup>4</sup> (unlike Ar+HF). As an example, the Ne+Na<sub>2</sub> system, having almost the same reduced mass as Ar+HF, can be interpreted on the basis of rotational rainbow structure<sup>5</sup> using the infinite-order sudden approximation (IOSA) and hard-shell models.<sup>6</sup> However, Ar+HF scattering appears to be significantly more complicated than systems examined previously. For example, no recognizable rainbow structure, attractive or repulsive, has yet been resolved for Ar+HF scattering.<sup>1,2,7</sup> Furthermore, the large rotational energy spacing for HF violates the energy sudden component of the IOSA.<sup>8</sup> Our earlier work<sup>2</sup> showed that the IOSA, while giving DCS qualitatively similar to the exact results, was quantitatively inaccurate. We have investigated the origin of this discrepancy in a separate study<sup>9</sup> and find that the energy sudden approximation is, indeed, the culprit. Thus, in order to investigate this system, we

must abandon the IOSA, with its computational simplicity, and use a more appropriate dynamical method.

Our earlier computational work showed that at least some of the observed features of the DCS are due to the attractiveness of the potential energy surface for Ar+HF and to its substantial anisotropy.<sup>2</sup> The goal of our present study is to further elucidate the origin of the most pronounced DCS features and to investigate how such features probe specific regions of the potential energy surface for Ar+HF scattering. In particular, it would be very helpful if some of the novel quantum features found in our earlier study could be connected to specific regions of the potential energy surface, as much as rotational rainbow structure has been connected to the repulsive wall in such systems as Ne+Na<sub>2</sub>.<sup>6</sup>

As in our earlier work,<sup>2</sup> we focus attention on the elastic  $j=0 \rightarrow j'=0$  and the weakly inelastic  $j=0 \rightarrow j'=1$  DCS. At a collision energy of 135 meV, chosen to mimic the experimental measurements,<sup>1</sup> the  $j=0 \rightarrow j'=0$  DCS shows a broad shoulder centered at a scattering angle of  $\theta \approx 60^\circ$  in the center-of-mass (c.m.) frame. In the same region, the  $j=0 \rightarrow j'=1$  DCS shows a sharp minimum that is very sensitive to the potential surface.<sup>2</sup> In the present work, we use only Hutson's “H6” surface for HF in its ground vibrational state  $v=0$ .<sup>3</sup>

The quantum close-coupling (CC) calculations reported here were performed using the Hibridon scattering package,<sup>10</sup> as discussed in our earlier work.<sup>2</sup> The CC calculations show rapid quantum diffraction oscillations<sup>11</sup> having periods of  $< 2^\circ$ , which we remove (using a  $2^\circ$ -wide smoothing function) simply to avoid obscuring broader DCS features.

In this paper, we present semiclassical (classical path) calculations in an attempt to investigate the novel scattering features seen earlier. In order to elucidate the quantum origin of the effects, we compare these semiclassical results

with their classical limit. Both semiclassical and classical methods are described in Sec. II. Results from these calculations are discussed in Sec. III and lead us to consider a time-dependent model calculation in Sec. IV. Finally, we summarize the insights gained from the semiclassical and model calculations in Sec. V. We devote close attention to connecting our understanding of the scattering features to particular aspects of the potential surface and discuss the utility of these connections for improving the potential surface.

## II. CALCULATIONS

### A. Semiclassical method

We use the traditional Jacobi coordinates to treat the dynamics. The HF bond vector is  $\mathbf{r}$  and the displacement of the Ar atom to the HF center of mass is  $\mathbf{R}$ . Because of the relatively light HF reduced mass, we treat the rotational states of the diatom quantum mechanically by expansion in a rigid rotor (spherical harmonic) basis set over  $\hat{\mathbf{r}}$ . Taking advantage of the heavy collisional reduced mass, we treat the translational motion in  $\mathbf{R}$  classically using a self-consistent field approach.<sup>12</sup> The Ar+HF potential is made time dependent through the translational coordinate  $V[\mathbf{R}(t), \mathbf{r}]$ . The time evolution of the system is calculated using the method of variation of parameters.<sup>13</sup> The approach is very similar to the traditional impact parameter method proposed by Mott<sup>14</sup> and by Bates.<sup>15</sup> However, we make no simplifying assumption for the classical trajectory. Such "classical path" models have been used extensively in the past and several excellent reviews of the subject are available.<sup>16</sup>

While the disadvantages of a mixed dynamics approach are well known,<sup>16,17</sup> we feel they are outweighed by the advantages for this particular case. Since the energy spacing of the HF ( $j=0$ ) and HF ( $j=1$ ) states is relatively small ( $41.12 \text{ cm}^{-1}$ ) compared with the translational energy ( $1089 \text{ cm}^{-1}$ ), the lack of energy conservation in the classical coordinate was not found to be of great significance. While the translational degree of freedom could certainly have been treated using wave packet methods, it is not clear that the considerable increase in computational effort would have significantly affected the outcome of the full calculation. Finally, we did attempt a fully consistent calculation using the Miller-Marcus semiclassical  $S$ -matrix theory.<sup>18,19</sup> However, the difficulties involved in incorporating the necessary phase information were formidable. (A very recent study<sup>20</sup> has, in fact, used this approach to explain quantum effects in Ar+HBr inelastic scattering.) Therefore, while the current approach has known deficiencies, we feel its computational ease, in combination with the dynamical insight yielded, outweighs these concerns. It should be noted that similar methods have been employed recently with great success in surface scattering<sup>21</sup> and in predissociation of van der Waals complexes.<sup>22</sup> Mixed dynamics methods have also been used to calculate state-to-state differential cross sections for vibrationally inelastic collisions<sup>23</sup> and to study fine structure transitions in atom-atom scattering.<sup>24</sup> In considering the

validity of the semiclassical model later in this paper (Sec. III), we will compare the results of the semiclassical dynamics to those from the exact quantum calculations which we carried out earlier.<sup>2</sup>

The classical (Hamilton's) equations of motion of Ar relative to the HF center of mass are given in Cartesian coordinates by

$$\dot{\mathbf{R}} = \frac{\mathbf{P}_R}{M}, \quad \dot{\mathbf{P}}_R = -\langle \nabla_R V(\hat{\mathbf{R}}, \hat{\mathbf{r}}) \rangle, \quad (1)$$

where  $M$  is the reduced mass of the collision system and the expectation value is over the angular coordinates of  $\mathbf{r} = (r, \theta, \phi)$  for HF at a fixed  $\mathbf{R}$ . The quantum mechanical equations of motion are

$$i\hbar \dot{c}_k(t) = \sum_l c_l(t) V_{kl}(t) \exp(i\omega_{kl}t), \quad (2)$$

where  $|l\rangle$  and  $|k\rangle$  denote the rigid rotor states  $|j, m\rangle$  and  $|j', m'\rangle$ , respectively;  $\omega_{kl} = (E_k - E_l)/\hbar$  and  $c_l(t) = \langle l | \Psi(t) \rangle = \langle Y_{jm} | \Psi(t) \rangle$  are the expansion coefficients. The potential matrix elements  $V_{kl}$  are given by

$$V_{kl} = \langle k | V(\hat{\mathbf{R}}, \hat{\mathbf{r}}) | l \rangle. \quad (3)$$

This becomes  $V_{kl}(t)$  through the time dependence of  $\mathbf{R}$  from Eq. (1). In this study, we focus on transitions from initial state  $j=0, m=0$  to final states  $j'$ . Since we are concerned only with level-to-level transitions, the probability of scattering into the  $j'$  rotational level, as a function of time, is given by

$$P_{j'}(t) = P_{0 \rightarrow j'}(t) = \sum_{m'=-j'}^{j'} |\langle j' m' | \Psi(t) \rangle|^2. \quad (4)$$

At a given impact parameter  $b$ , a classical trajectory was started at a large distance from the diatom and allowed to evolve to large times. For each  $b$ , the final scattering angle  $\theta$  given by  $\theta = \arccos[\mathbf{P}_R(t=0) \cdot \mathbf{P}_R(t=\infty)]$  is obtained along with the level-to-level quantum mechanical transition probability  $P_{j'}(t \rightarrow \infty; b)$ . Since we are dealing with heavy scattering particles, differential cross sections are calculated using the classical deflection function  $\theta(b)$  and  $P_{j'}(b)$  using the equation

$$\frac{d\sigma_{j'}(\theta)}{d\omega} = \frac{1}{\sin \theta} \sum_i b_i \left| \frac{d\theta}{db} \right|_{b_i}^{-1} P_{j'}(b_i). \quad (5)$$

As in the standard classical treatment of elastic scattering,<sup>25</sup> the sum is over all impact parameters which contribute to the same value of  $\theta$ .  $P_{j'}(b_i)$  is the quantum mechanical probability of finding the system in the final rotational state  $j'$  for each such impact parameter  $b_i$ . The errors involved in this approximation have been discussed previously.<sup>26</sup> In particular, the greatest sacrifice is the loss of interference information between the partial waves at each orbital angular momentum. For instance, rainbow scattering will be represented by, at best, a primitive semiclassical picture, in which the DCS at the rainbow angle shows a singularity.<sup>27</sup> Furthermore, such features as diffraction oscillations will not be observed. Since the latter phenomenon is not yet experimentally resolvable, its loss is

not significant for the present analysis. As will be shown in Sec. III, the quantum features observed in the DCS for  $j'=0$  and 1 do not arise from this type of interference.

### B. Classical mean field trajectory method

In order to compare the purely classical time evolution of the system with that of the semiclassical method just discussed, we use the classical mean field technique.<sup>28</sup> Rather than computing several trajectories with random initial orientation individually and averaging to obtain the desired scattering data,<sup>29</sup> a “swarm” of trajectories are run simultaneously at a single impact parameter. This swarm randomly samples the initial diatom orientation space, as required for an atom–rigid rotor collision. The equations of motion for the mean field trajectories are

$$\dot{\mathbf{p}}_i = -\nabla_r V(\hat{\mathbf{R}}, \hat{\mathbf{f}}_i), \quad \dot{\mathbf{r}}_i = \mathbf{p}_i/\mu, \quad (6a)$$

$$\dot{\mathbf{P}}_R = -\langle \nabla_R V(\hat{\mathbf{R}}, \hat{\mathbf{f}}) \rangle_r, \quad \dot{\mathbf{R}} = \mathbf{P}_R/M, \quad (6b)$$

where the subscript  $i$  denotes the  $i$ th classical trajectory. The symbol  $\langle \rangle_r$  in Eq. (6b) denotes the ensemble average over each trajectory in the swarm. As before,  $M$  is the collisional reduced mass and  $\mu$  is the diatom reduced mass. The vectors  $\mathbf{r}_i$  and  $\mathbf{p}_i$  are the diatom displacement and momentum, respectively. By propagating the relative motion in the mean field of the potential, we ensure that the only difference between the dynamics of the mean field trajectory and the semiclassical methods is the quantum nature of the rotational state evolution.

During the course of integrating the trajectory swarm, the current “rotational state” of the diatom may be calculated for each of the individual trajectories by the relation

$$\tilde{\mathbf{J}}_i = \mathbf{r}_i \times \mathbf{p}_i, \quad (7)$$

where  $\tilde{\mathbf{J}}_i$  is the continuous rotational angular momentum of the diatom of the  $i$ th trajectory. By using an appropriate binning method, one can determine the rotational state probability of the classical system at any time  $t$ . The  $i$ th trajectory contributes to the  $j$ th rotational bin if  $j - \frac{1}{2} \leq |\tilde{\mathbf{J}}_i| < j + \frac{1}{2}$ . The classical rotational state probability  $\mathcal{P}_j^{\text{cl}}$  is given by

$$\mathcal{P}_j^{\text{cl}}(t; b) = \frac{N_j(t)}{N}, \quad (8)$$

where  $N$  is the total number of trajectories in the swarm at a given  $b$  (typically  $N=100$ ) and  $N_j(t)$  is the number of trajectories in the  $j$ th bin at some time  $t$ .

The classical opacity function is given by  $\mathcal{P}_j^{\text{cl}}(t; b)$  as  $t \rightarrow \infty$ . The classical DCS are calculated by Eq. (5), just as are the semiclassical DCS, only now we use the classical opacity function,  $\mathcal{P}_j^{\text{cl}}(b)$ . This permits a direct comparison between the classical and semiclassical models of the scattering dynamics.

### III. RESULTS AND DISCUSSION

Classical and semiclassical deflection functions and opacity functions for  $j'=0, 1$ , and 2 are shown in Fig. 1.

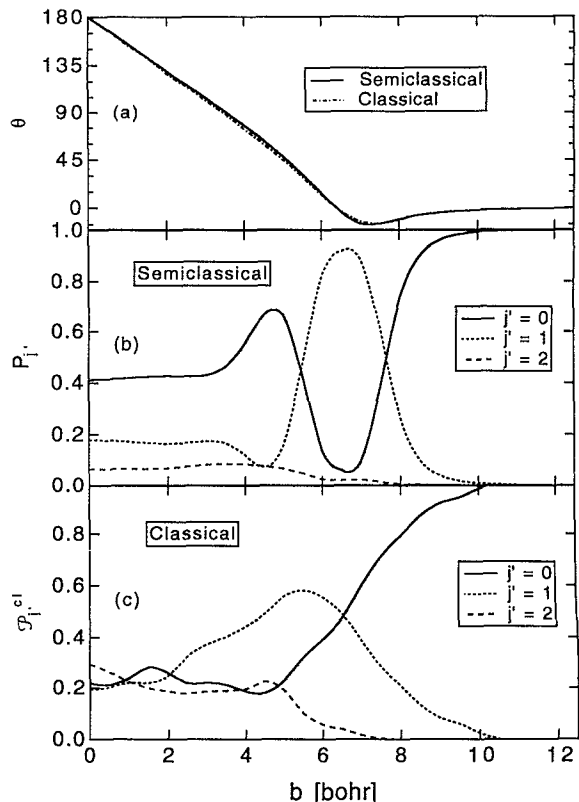


FIG. 1. Deflection and opacity functions from semiclassical and classical trajectory calculations. Plotted are (a) the scattering angle  $\theta$ ; (b) semiclassical final rotational state probability  $P_{j'}$ ; and (c) classical final rotational state probability  $\mathcal{P}_{j'}^{\text{cl}}$ , as a function of the impact parameter  $b$ . The initial rotational state is  $|j=0, m=0\rangle$ . Relative collision energy is 135 meV.

The classical and semiclassical deflection functions are so close that any differences in the corresponding DCS must be due almost exclusively to their opacity functions. The lower two panels of Fig. 1 do indeed show striking differences between them. The semiclassical results show weak probabilities into  $j' \geq 2$ , so that the  $j'=0$  and  $j'=1$  probabilities are almost “mirror images” of each other. This is most clearly seen in the oscillatory structure for the impact parameter range of  $b \sim 3$ –8 bohr. In contrast, the classical results show no such strong coupling between the  $j'=0$  and  $j'=1$  states, and there is no similar oscillatory structure at all; the classical opacity function for  $j'=0$  shows essentially a monotonic increase of  $\mathcal{P}^{\text{cl}}(b)$  for  $b > 4$  bohr.

The semiclassical cross sections obtained from Eq. (5) are shown in Fig. 2. They are also compared with the purely classical calculations and with the “exact” quantum close-coupled DCS obtained earlier.<sup>2</sup> It is immediately clear that the semiclassical DCS reproduce qualitatively all features of the close-coupled DCS except for the  $j=0 \rightarrow j'=1$  DCS below  $\theta=20^\circ$ . We will discuss the DCS in this angular region later in this section. We now concentrate on the  $j=0 \rightarrow j'=0$  “shoulder” and the  $j=0 \rightarrow j'=1$  “hole” features near  $\theta=60^\circ$ , which we identified in an earlier publication as quantum mechanical in origin.<sup>2</sup> From Fig. 1, we can see that this scattering angle

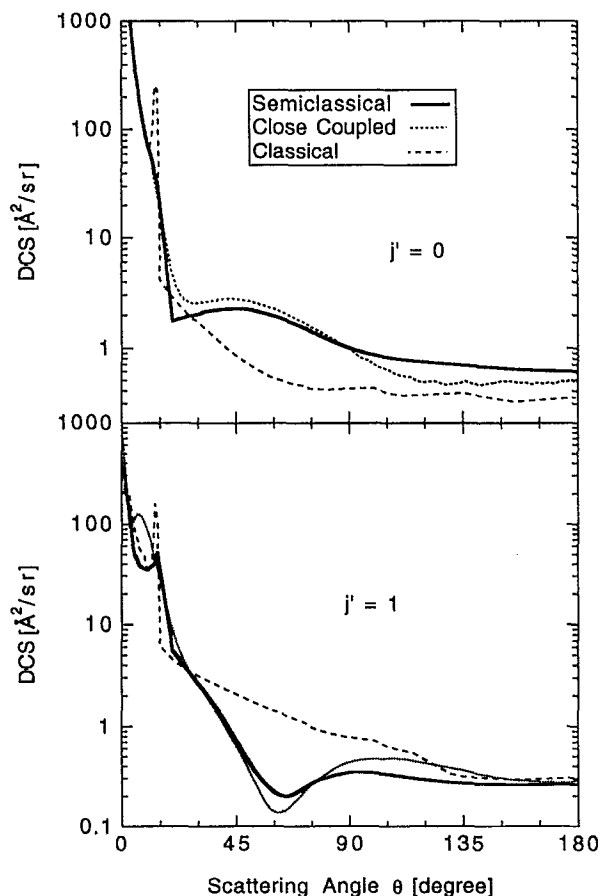


FIG. 2. Differential cross section (DCS) from converged close coupled (Ref. 2), semiclassical, and classical calculations for final rotational states  $j'=0$  and  $j'=1$ .

corresponds to an impact parameter of  $b \sim 4.5$  bohr. This is just where the semiclassical  $0 \rightarrow 0$  probability goes through a local maximum, with a corresponding minimum in the  $0 \rightarrow 1$  probability. The  $0 \rightarrow 0$  shoulder and  $0 \rightarrow 1$  hole therefore are seen to be complementary features that are present in the CC and semiclassical dynamics, but altogether absent at the fully classical level. The order-of-magnitude difference between the classical and close-coupled DCS of Fig. 2 is a consequence of the divergence of the classical and semiclassical opacity functions in the narrow range of impact parameters near  $b \sim 4.5$  bohr.

Using the classical relation  $l = Mvb$  (where  $l$  is the orbital angular momentum and  $v$  is the collision velocity), the range of impact parameters near  $b \sim 4.5$  bohr corresponds to  $l \sim 70\hbar$ . Because so little angular momentum is due to the HF rotation, the region of greatest interest is for total angular momenta near  $J = 70\hbar$ . This is just where the CC calculations show their greatest sensitivity to the potential energy surface.<sup>2</sup> The quantum effects identified earlier also arise from this  $J$  range.<sup>2</sup> The correspondence between the CC and semiclassical results in this range of  $J$ 's and  $b$ 's arises because of the quantum treatment of the HF rotor in the semiclassical model. This suggests that the potential surface, in its role of coupling the rotational states, makes significant contributions to both the existence

and location of these quantum features. Conversely, such features in the DCS should provide valuable information on the exact nature of the potential energy surface.

Returning now to the region of scattering angles below  $\theta = 20^\circ$ , we see virtually perfect agreement between the semiclassical and CC results for the  $j'=0$  DCS, in contrast to a very strong peak in the classical DCS at  $\theta = 13^\circ$ . The latter is clearly identified with the minimum seen for the classical deflection function in Fig. 1(a), yielding a classical rainbow infinity due to the  $|d\theta/db|^{-1}$  factor in Eq. (5). Although the semiclassical calculation shares this minimum in the deflection function, the  $0 \rightarrow 0$  probability in Fig. 1(b) is so low that the rainbow is quenched, beautifully reproducing the close-coupled DCS. A consequence of the  $0 \rightarrow 0$  minimum in the semiclassical probability is the  $0 \rightarrow 1$  maximum, which therefore produces a pronounced maximum in the semiclassical  $j'=1$  DCS. The inelastic  $0 \rightarrow 1$  rainbow has essentially completely quenched the elastic  $0 \rightarrow 0$  rainbow, thus preventing observation of a strong rainbow in the rotationally unresolved DCS experiments of Vohralik *et al.*<sup>7</sup> That this rainbow is shifted to a larger scattering angle relative to the close-coupled DCS is known from other comparisons of primary rainbows in classical and quantum mechanics.<sup>30</sup>

The above discussion allows assignment of the feature near  $|\theta| = 10^\circ$  as an  $l$ -type rainbow.<sup>6,31</sup> The sudden drop of signal from the "bright" to the "dark" side of the rainbow beyond  $|\theta| = 13^\circ$  in the classical and semiclassical DCS is also well known.<sup>27</sup> It is due to three impact parameter contributions to Eq. (5) for  $|\theta| < 13^\circ$  switching to only one contribution for  $|\theta| > 13^\circ$ .

In our earlier publication,<sup>2</sup> we also gave close-coupled DCS for scattering of  $\text{Ar} + \text{DF}$  ( $j=0$ )  $\rightarrow$   $\text{Ar} + \text{DF}$  ( $j'=0,1$ ) for comparison to the HF scattering. Figure 3 displays such a comparison for the present semiclassical results. Away from the rainbow region, we find again that the semiclassical results are very similar to the CC cross sections (not shown here). In particular, the striking dissimilarities between  $\text{Ar} + \text{DF}$  and  $\text{Ar} + \text{HF}$  scattering are reproduced faithfully. The "shoulder" at  $\theta = 60^\circ$  for HF ( $j'=0$ ) is replaced by a "dip" near  $\theta = 30^\circ$  for DF; similarly, the HF ( $j'=1$ ) dip becomes a shoulder for DF ( $j'=1$ ). We seek an explanation for these changes in the opacity functions for  $\text{Ar} + \text{DF}$  scattering.

Figure 4 shows a comparison of  $\text{Ar} + \text{DF}$  and  $\text{Ar} + \text{HF}$  opacity functions. Since the translational reduced mass is hardly affected by the H  $\rightarrow$  D isotopic substitution, there is relatively little change in the classical deflection function, which remains indistinguishable from that shown in Fig. 1(a). Examination of the opacity functions reveals them to be qualitatively similar to the HF results. The probabilities for  $\text{Ar} + \text{DF}$  are also oscillatory and the  $0 \rightarrow 0$  and  $0 \rightarrow 1$  opacity functions still mirror each other, despite larger probabilities for  $\text{Ar} + \text{DF}$  ( $j' \geq 2$ ). However, the  $0 \rightarrow 0$  maximum has shifted to lower impact parameters from  $b \sim 4.5$  to  $\sim 3.6$  bohr and has broadened, moving the  $\text{Ar} + \text{DF}$  shoulder substantially outward in scattering angle (and significantly weakening it). Simultaneously, there is very little  $0 \rightarrow 0$  probability in the entire impact parameter range

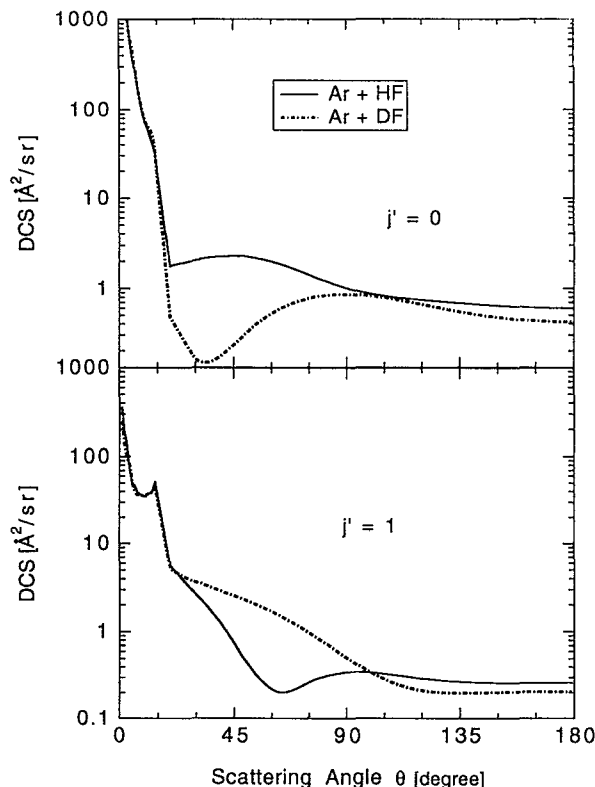


FIG. 3. Differential scattering cross sections for Ar+HF and Ar+DF. Initial rotational state and collision energy are the same as those in Fig. 1. Only the semiclassical results are shown.

of  $b \sim 5\text{--}7$  bohr, corresponding to the DCS minimum seen near  $\theta \sim 30^\circ$ . The Ar+DF  $0 \rightarrow 1$  opacity function no longer has a minimum at  $b \sim 4.5$  bohr, so there is no “hole” like that seen in the DCS for Ar+HF scattering. Instead, the monotonic  $0 \rightarrow 1$  probability for  $b$  in the range  $3.0\text{--}7.0$  bohr

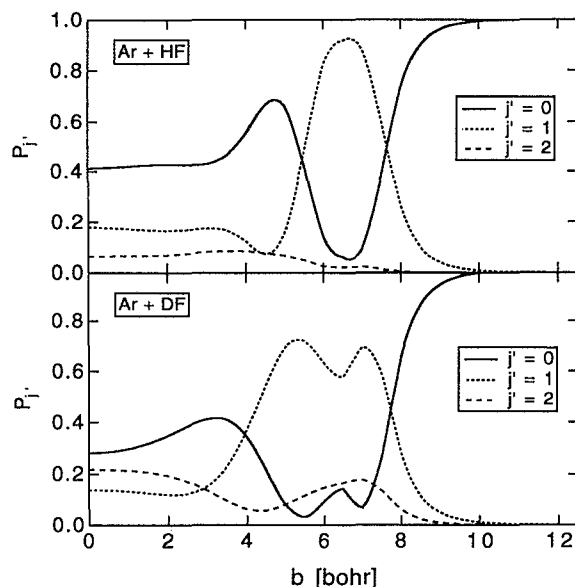


FIG. 4. Opacity functions for Ar+HF and Ar+DF.

fills in the entire DCS for Ar+DF scattering from  $\theta \sim 30^\circ\text{--}90^\circ$ . It is seen that shifts in the details of the opacity functions for Ar+DF scattering are sufficient to completely alter the DCS shown in Fig. 3.

Excellent agreement between the semiclassical (classical path) results and close-coupled DCS (Fig. 2) justifies the use of the former approach. We now utilize the time-dependent aspect of these calculations to investigate the role played by the potential in producing the DCS shown in Figs. 2 and 3. To that end, we introduce a model calculation for the insight it yields into the details of the collision dynamics.

#### IV. THE ROLE OF THE INTERMOLECULAR POTENTIAL: MODEL CALCULATION

To exploit the full power of the semiclassical method, we now utilize the time-dependent aspect of the calculation to explore the scattering dynamics. In Fig. 5, we show the quantum mechanical time evolution of  $P_{j'}$  for various impact parameters. It is clear that there is strong coupling between the  $j=0$  and 1 states at all times; indeed it is the  $t \rightarrow \infty$  manifestation of this coupling which is observed in the semiclassical opacity functions of Fig. 1. At a high impact parameter, this coupling is not surprising since, as observed above, states with  $j' > 1$  have little probability; i.e.,  $P_0$  and  $P_1$  sum to approximately unity. At low impact parameter, higher  $j'$  states are populated, but the sum of their probabilities is essentially decoupled from the  $j'=0$  and 1 probabilities. For clarity, the probabilities into other states are not shown in Fig. 5. However, no obvious coupling pattern was observed for these higher rotational states.

Noting the coupling between the  $j=0$  and 1 rotational states, we attempt to examine the dynamics of the rotational energy exchange using a simplified two-state model. We choose these states to be  $|0,0\rangle$  and  $|1,0\rangle$ . The justification for this choice will be given in some detail later. The potential matrix elements  $\langle 0,0 | V[\mathbf{R}(t), \hat{\mathbf{f}}] | 0,0 \rangle = V_{00}(t)$  and  $\langle 0,0 | V[\mathbf{R}(t), \hat{\mathbf{f}}] | 1,0 \rangle = V_{01}(t)$  are shown in Fig. 6 for several impact parameters. Since all the diagonal matrix elements  $\langle k | V(t) | k \rangle$  are similar (not shown in Fig. 6), we set  $V_{11} = V_{00}$  in our model calculation. Also, since  $V_{01}(t)$  is much less than  $V_{00}(t)$ , but qualitatively similar in form, we model  $V_{01}(t)$  as  $\epsilon V_{00}(t)$ , where  $\epsilon$  is a constant less than 1. Finally, we impose the energy sudden approximation by setting  $\omega_{01} = 0$ , corresponding to degenerate rotational energy levels. In this model, the quantum equations of motion, given for the full system in Eq. (2), reduce to

$$i\hbar \dot{c}_0(t) = V_{00}(t) [c_0(t) + \epsilon c_1(t)], \quad (9a)$$

$$i\hbar \dot{c}_1(t) = V_{00}(t) [\epsilon c_0(t) + c_1(t)]. \quad (9b)$$

These simplifications allow us to examine several different coupling cases (weak, intermediate, and strong) through the variation of a single parameter  $\epsilon$ , which is a measure of the potential energy coupling between the rotational states. We employ the initial conditions  $c_0(0) = 1$  and  $c_1(0) = 0$ . The relative collision energy is 135 meV, as was used in the full treatments. The  $V_{00}(t)$ 's are taken from these runs.

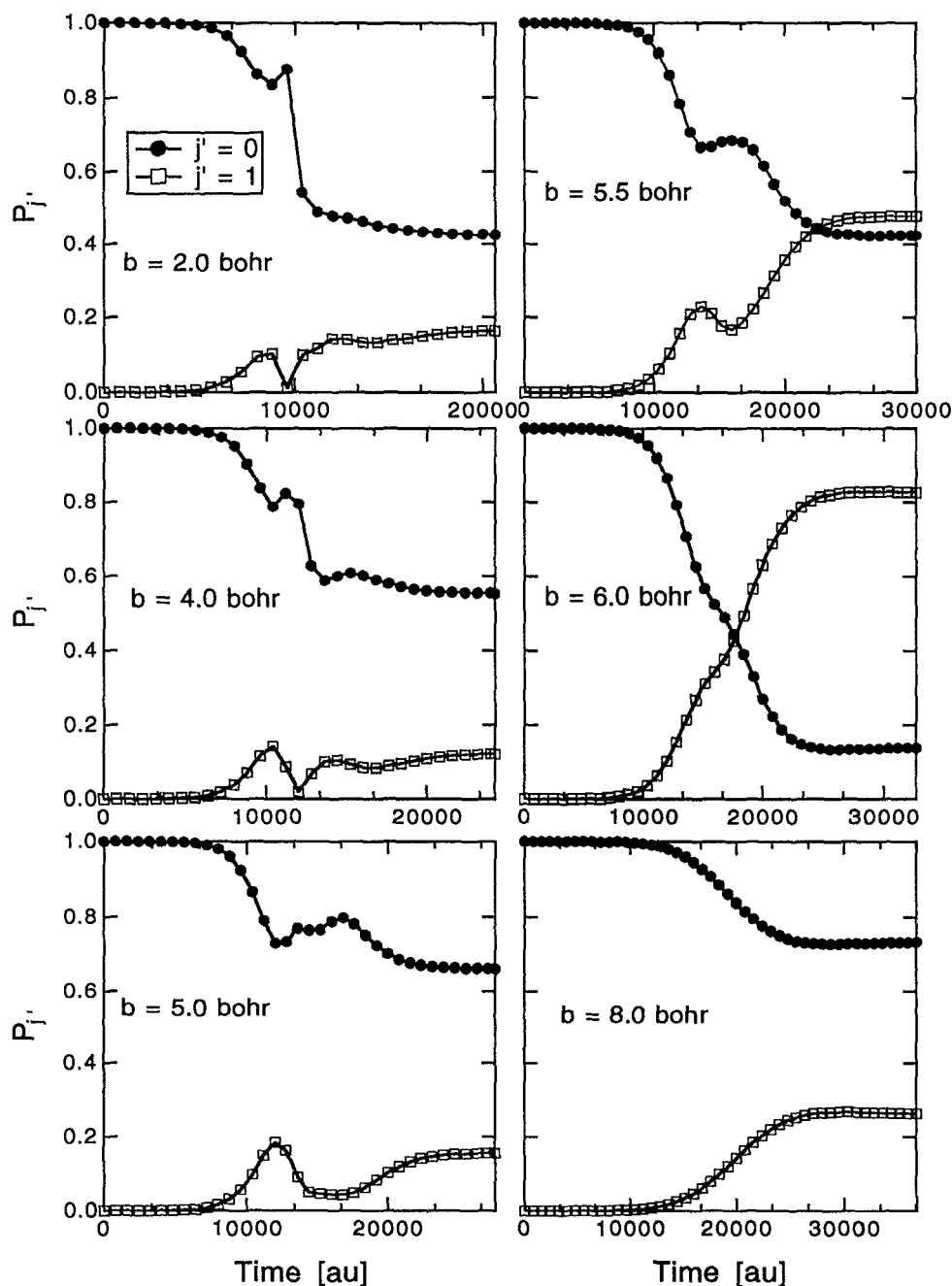


FIG. 5. Time-dependent rotational state probabilities from semiclassical calculation at several impact parameters  $b$ . Initial rotational state is  $j=0$ ; relative collision energy is 135 meV. Note that the time scales in Figs. 5 and 6 vary with  $b$ . This is done to locate the turning point in the translational motion near the midpoint of the time axis (Fig. 5) and to emphasize the symmetry of the time-dependent potential (Fig. 6).

Using this two-state model, the internal state dynamics reduces to the time evolution of the coefficients  $c_0(t)$  and  $c_1(t)$ . We plot trajectories of these expansion coefficients in the complex plane in Figs. 7–9 for various values of  $b$  and  $\epsilon$ . In order to gain insight into the meaning of these plots, we note first that for  $\epsilon=0$  (i.e., no coupling between  $j=0$  and 1), the equations of motion (9) become

$$\dot{c}_i = \frac{-ic_i V_{00}}{\hbar} \quad (i=0,1). \quad (10)$$

By writing  $c_i = |c_i| \exp(i\phi_i)$ , where  $\phi_i = \arg(c_i)$ , substituting into Eq. (10), and equating the real and imaginary parts, we obtain

$$\frac{d}{dt} |c_i| = 0, \quad \frac{d}{dt} \phi_i = \frac{-V_{00}}{\hbar} \quad (11)$$

with the explicit result that

$$c_i(t) = c_i(0) \exp \left[ -i \int_0^t dt' V_{00}(t') / \hbar \right] \quad (12)$$

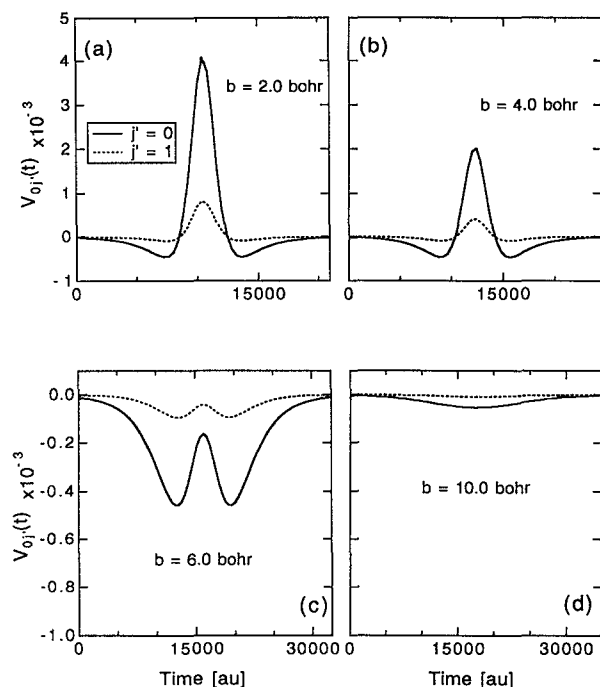


FIG. 6. Time-dependent coupling elements  $V_{00}(t)$  and  $V_{01}(t)$  at several impact parameters  $b$ .

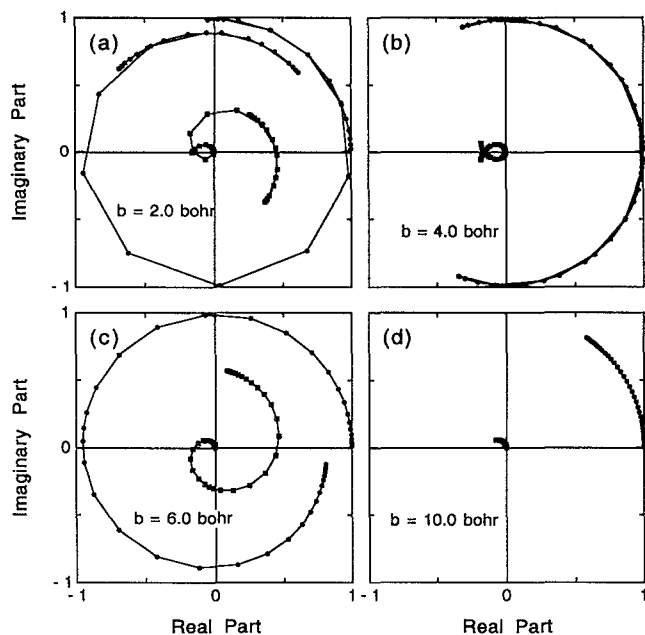


FIG. 7. A plot of time-dependent expansion coefficients  $c_0$  (filled circles) and  $c_1$  (open squares) in the complex plane for the two-state model calculation  $\epsilon=0.1$ . At time  $t=0$ ,  $c_0=(1,0)$  and  $c_1=(0,0)$ . The initial sense of motion is a spiral in the counterclockwise direction. The sampling rate for positive potential elements [i.e., for clockwise rotation (see the text)] is four times that for negative coupling elements.

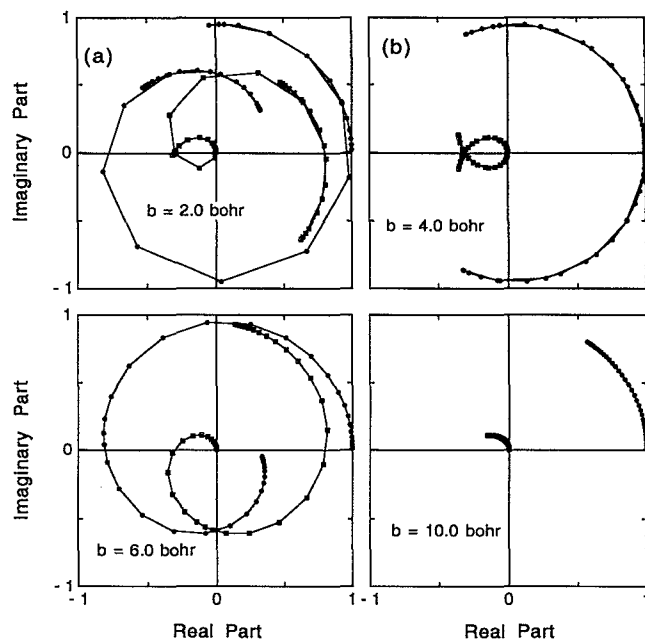


FIG. 8. The same as Fig. 7 except  $\epsilon=0.2$ .

gives the time evolution for the states. The integral in Eq. (12) is known as the action integral. Thus motion in the  $\epsilon=0$  case is pure rotation in the complex plane. A negative  $V_{00}$  leads to counterclockwise rotation in the complex plane; a positive  $V_{00}$  gives clockwise rotation.

Consider next the effect of the off-diagonal terms in Eq. (9). In general, if  $c_i$  is itself negligible, then the time evolution of  $c_i$  is governed by the present value of  $c_j$  ( $j \neq i$ ). The equations of motion reduce to

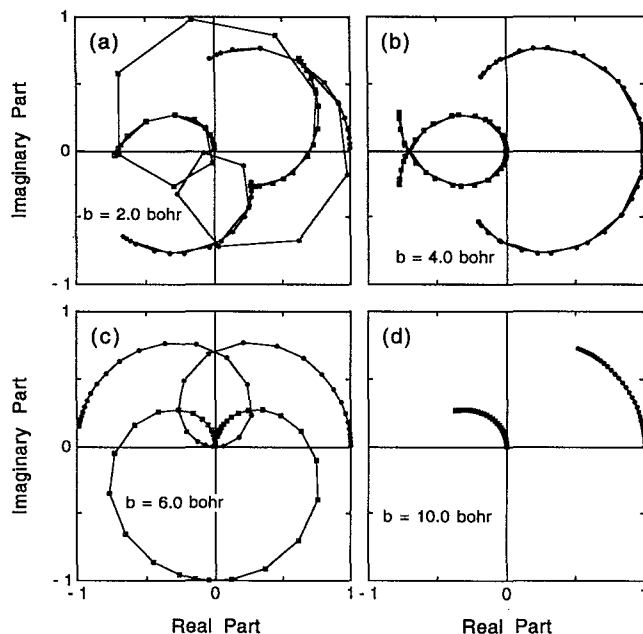


FIG. 9. The same as Fig. 7 except  $\epsilon=0.5$ .



$$\dot{c}_i(t) = (i\hbar)^{-1} \epsilon V_{00}(t) c_j(t) \quad (j \neq i), \quad (13)$$

or

$$\begin{aligned} \delta c_i(t) &= \dot{c}_i(t) \delta t = [\delta t \hbar^{-1} \epsilon V_{00}(t) |c_j(t)|] \exp[i(\phi_j - \frac{\pi}{2})] \\ &= \{\delta t \hbar^{-1} \epsilon |V_{00}(t)| |c_j(t)|\} \\ &\quad \times \exp[i(\phi_j - \text{sign}[V_{00}(t)]\pi/2)]. \end{aligned} \quad (14)$$

The term within the braces is always positive. Thus, the change in  $c_i$  due to a nonzero  $c_j$  is a complex number rotated  $\pi/2$  from  $c_j$  either clockwise or counterclockwise depending on the sign of  $V_{00}$ . The amplitude of  $\delta c_i$  is, of course, governed by  $\epsilon$ .

The easiest plots to analyze are those for the large impact parameter case. For  $b \gg 6$  bohr,  $V_{00}$  is never positive (see Fig. 6), and therefore the sense of rotation in the complex plane is always counterclockwise. This is clearly shown for  $b = 6.0$  bohr in Figs. 7–9(c). Here  $c_0(0) = (1, 0)$  and  $c_0$  spirals inward as a function of time. Simultaneously,  $c_1$  spirals outward from  $(0, 0)$ . Since  $V_{00}(t)$  is always negative, the rotation is counterclockwise. The points on the figures are sampled at evenly spaced time steps. Thus, the separation of points indicates the rate of rotation in the complex plane, and hence, the magnitude of  $V_{00}$ . At first closely spaced, the points become more widely spaced as the classical trajectory samples the most attractive part of the potential. Then the spacing closes up as  $|V_{00}|$  approaches zero near the classical turning point. The attractive well region is traversed again as the particles separate, resulting in acceleration and finally, as  $R$  becomes large, deceleration of the angular motion in the complex plane. At this impact parameter, it can also be seen that the classical turning point occurs near  $c_0 = (-1, 0)$  for the low ( $\epsilon = 0.1$ ) and intermediate ( $\epsilon = 0.2$ ) coupling cases.

The effect of changing  $\epsilon$  can be seen by comparing the panels for  $\epsilon = 0.1, 0.2$ , and  $0.5$  at the same value of  $b$ . The effect is particularly obvious at high  $b$  [Figs. 7–9(d)]. Clearly,  $\epsilon$  controls the radial velocity at which  $c_1$  spirals out from  $(0, 0)$ . Note that at times near  $t = 0$ , when  $c_0 \approx (1, 0)$  that  $\delta c_1$  lies along  $(0, 1)$ ; i.e.,  $\delta c_1$  is rotated  $\pi/2$  rad counterclockwise from  $c_0$ , as predicted by Eq. (14).

As is clear from Fig. 6, the magnitude of  $V_{00}(t)$  decreases as the impact parameter increases from 6 to 10 bohr. The role of the  $V_{00}$  potential in the dynamics is seen by examination of Figs. 7(c), 7(d), 8(c), 8(d), 9(c), and 9(d). The smaller the magnitude of  $V_{00}(t)$ , the less  $c_0$  rotates from its starting value of  $(1, 0)$ . Therefore, for  $b = 10$  bohr, we see  $c_0$  rotates only  $60^\circ$ , compared with the  $350^\circ$  rotation attained for  $b = 6$  bohr in the weak and intermediate coupling cases. (The pattern in the strong coupling case  $\epsilon = 0.5$  is, as might be expected, more complicated and will be discussed later.)

Since the sense of rotation of  $c_1$  is also governed by  $V_{00}$ , it is not surprising that the modulus of  $c_1$  is influenced by the magnitude of  $V_{00}$ ; the more “time” available for rotation in the complex plane, the farther  $c_1$  can spiral out from the origin. In both the  $\epsilon = 0.1$  and  $\epsilon = 0.2$  cases this can be seen by comparing panels 7(c) and 7(d) and 8(c) and 8(d). In the  $b = 6$  bohr case,  $c_1$  has time to spiral

TABLE I. A comparison of the action along the classical path  $\int V_{00} dt$  and final value of the argument of the  $c_0$  coefficient in the complex plane for the  $\epsilon = 0.2$  case. Note the “balanced” trajectory, at  $b = 4.0$  bohr, has an action and  $\arg(c_0)$  of  $\sim 0$ .

$b$ (bohr)	$\int V_{00} dt$ ( $\hbar$ )	$-\arg[c_0(\infty)]$ (radian)
0	0.2676	5.356
2	0.2037	4.192
4	0.0092	0.2161
6	-0.3065	-6.128
8	-0.1882	-3.761
10	-0.0478	-0.9550
12	-0.0167	-0.3314

outward and reach a significant nonzero value of  $|c_1|$ ; for  $b = 10$  bohr, this is not the case. Thus, the magnitude of the  $V_{00}$  potential is a significant factor in determining the transition probability. The ability to rotate about the origin is a measure of the strength of the potential. It is closely related to the action  $\int V_{00}(t) dt$ . In Table I, we compare this measure of the rotation  $\arg[c_0(\infty)]$  and the action. (Note that the arguments given in Table I are not modulo  $2\pi$ ; rotation in the complex plane often goes onto neighboring Riemann sheets. The branch cut is along the real axis.) Clearly, both these measures diminish as  $b$  increases past 8 bohr. As can be seen from Fig. 10, this is precisely the range of  $b$  values for which the  $0 \rightarrow 1$  transition probability monotonically decreases.

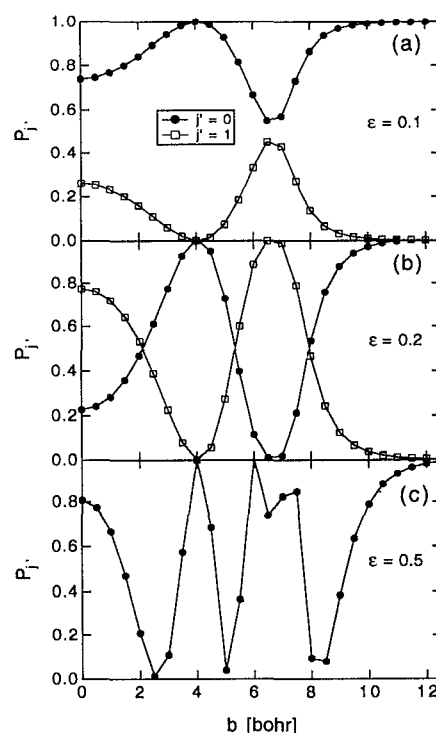


FIG. 10. Opacity functions from the two-state model calculation for  $\epsilon = 0.1, 0.2$ , and  $0.5$ . (c) Only the opacity function for  $j' = 0$  is shown for clarity; the opacity function for  $j' = 1$  is the complement of that shown.

These panels also illustrate the effect of increasing  $\epsilon$ . Clearly from Eq. (14),  $\epsilon$  gives a measure of the radial component of the motion. For  $b=10$  bohr, e.g., the "total rotation" (action) is the same in all cases, but the magnitude of the radial motion clearly scales with  $\epsilon$ .

Examination of the opacity functions (Fig. 10) for varying values of  $\epsilon$  illustrates the effect of  $\epsilon$  in coupling the two states as  $t \rightarrow \infty$ . As  $\epsilon$  is increased, the strength of the coupling between  $|0\rangle$  and  $|1\rangle$  is increased. This coupling appears as an oscillation in the opacity functions. The weakly coupled system ( $\epsilon=0.1$ ) shows only a slight oscillation in the opacity functions. By the time we get to the very strong coupling case ( $\epsilon=0.5$ ), the opacity functions are oscillating wildly. The origin of this strong oscillation can be gleaned from Figs. 7–9. In particular, consider Fig. 9(c). As in Figs. 7(c) and 8(c),  $V_{00}$  controls the angular motion and  $\epsilon$  controls the radial motion. In this particular case though, the coupling is so strong that  $c_0$  initially spirals very rapidly toward the origin. As the counterclockwise rotation continues, it loops back on itself in the upper half of the plane and spirals back out to a large  $|c_0|$ . Clearly then for large  $\epsilon$ , such closed loops will lead to a dynamics highly sensitive to the exact details of the potential.

Let us now examine the evolution of  $c_0(t)$  and  $c_1(t)$  at the lower impact parameters. It can be seen in Figs. 7–9(b) that for  $b < 6.0$  bohr, the rotation of  $c_0(t)$  reverses its direction during the collision. This is evidently the result of encountering the repulsive part of the potential. This reversal, as we pass from the attractive region to the repulsive on the incoming part of the trajectory, and the retracing of its path on the outgoing part, has the effect of bringing  $c_1(t)$  back toward the origin. That is, at lower values of  $b$ , the repulsive part of the potential favors the transition  $0 \rightarrow 1$ , but the attractive part of the potential after the turning point forces the system back into  $j'=0$ . However, as  $b$  becomes sufficiently large,  $V_{00}$  has no repulsive component. There is therefore no reversal of direction; hence no tendency for  $c_1$  to reverse back toward the origin. At these intermediate impact parameters ( $b=5$ –7 bohr), the attractive part of the potential favors the  $0 \rightarrow 1$  transition and we see the continuing outward spiral of the  $c_1(t)$  coefficient.

The actual average value of  $V_{01}/V_{00}$  for the  $H6$  potential (see Fig. 6) is near 0.2, where the opacity function behaves much less dramatically than in the  $\epsilon=0.5$  case. In fact, the model calculations for  $\epsilon=0.2$  nicely reproduce many of the features seen in the opacity functions for the full calculation. Therefore, we will use the model data for  $\epsilon=0.2$  to discuss the opacity functions of Fig. 1(b). The opacity function of Fig. 10(b) is qualitatively similar to that for the semiclassical data in Fig. 1(b). This semiquantitative agreement between the asymptotic results of the two-state model and the full run is our justification (albeit empirical) for the use of the model. By following detailed dynamics in several cases, we have established that the model is reasonable in the sense that  $P_0(t)$  in the model and full calculations are qualitatively similar for the appropriate choice of coupling parameter.

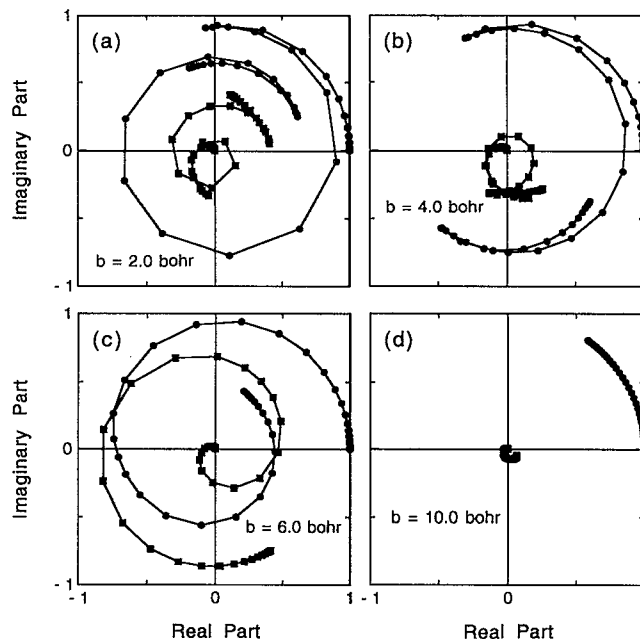


FIG. 11. A plot of expansion coefficients in the complex plane from full semiclassical model for states  $|j'=0, m'=0\rangle$  and  $|j'=1, m'=0\rangle$  at same impact parameters as those in Figs. 7–9. Initial state is  $|j=0, m=0\rangle$ ; relative collision is 135 meV.

The reason for the peak in the opacity function for  $j'=0$  at  $b=4.0$  bohr in the model calculation can be understood by examination of Fig. 8(b). It can be seen from this figure that  $c_0(t)$  returns to  $(1,0)$  twice during the collision. In fact, it is clear that the net action for this trajectory is almost exactly zero. That is, at this impact parameter, the attractive and repulsive parts of the potential exactly balance each other on the incoming and outgoing portions of the classical path. We can see that initially  $c_0(t)$  rotates counterclockwise until the repulsive part of the potential is reached. At this point,  $V_{00}(t)$  becomes positive and  $c_0(t)$  retraces its initial path. The rotation of  $c_0(t)$  continues to a point conjugate to the position where the repulsive part of the potential was entered. As the trajectory goes back into the attractive part of the potential, the cycle is completed by  $c_0(t)$  retracing its path once more back to  $(1,0)$ . It is this balancing between the attractive and repulsive parts of the potential (and the consequent peak in  $P_0$ ) that is responsible for the quantum feature seen near  $\theta=30^\circ$ – $60^\circ$  in the DCS for the full system. The generality of this zero action trajectory is apparent from examination of  $c_0(t)$  for  $\epsilon=0.1$  and  $0.5$  [Figs. 7(b) and 9(b)]. In all cases, the balance between the attractive and repulsive parts of the potential is observed and the trajectory retraces itself and returns to its  $t=0$  value.

Although the model calculation with  $\epsilon=0.2$  reproduces the full semiclassical data reasonably well at the level of the opacity function [Fig. 10(b)] requiring that the full calculation and the model agree as a function of time is more demanding. We therefore compare coefficients from a full run using Eq. (2) (Fig. 11) with those from the model calculation (Fig. 8). Clearly, from Figs. 8(c) and 8(d)

and 11(c) and 11(d), one difference is that  $c_1(t)$  rotates farther in the full calculation. This is due to the presence of the  $\omega_{01}$  term in the latter. Rewriting Eq. (2) for a two-level system yields

$$i\hbar\dot{c}_0(t) = c_0(t)V_{00}(t) + c_1(t)V_{01}(t)\exp(i\omega_{01}t), \quad (15a)$$

$$i\hbar\dot{c}_1(t) = c_0(t)V_{01}(t)\exp(-i\omega_{01}t) + c_1(t)V_{11}(t). \quad (15b)$$

Following our earlier analysis, for  $V_{01}=0$ , we find that  $c_i(t) = c_i(0)\exp[-i\int_0^t dt' V_{ii}(t')/\hbar]$ . Therefore, the overall rates of rotation in the complex plane are not affected by the  $\omega_{01}$  term.

On the other hand, if the effect of the diagonal terms is ignored, then Eqs. (15) simplify to

$$i\hbar\dot{c}_0(t) = c_1(t)V_{01}(t)\exp(i\omega_{01}t), \quad (16a)$$

$$i\hbar\dot{c}_1(t) = c_0(t)V_{01}(t)\exp(-i\omega_{01}t) \quad (16b)$$

yielding a change  $\delta c_i$  [cf. Eq. (14)]

$$\delta c_i(t) = [\delta t \hbar^{-1} |V_{01}(t)| |c_j(t)|] \times \exp\left[i\left\{\phi_j - \text{sign}[V_{01}(t)] \frac{\pi}{2} \pm \omega_{01}t\right\}\right], \quad (17)$$

where the plus(minus) sign applies for  $i=0(1)$ . One effect of this is to change the initial sense of rotation of  $c_1(t)$ . The initial motion of  $c_1(t)$  is now no longer along (0,1), but pushed somewhat into the second quadrant. This explains why  $c_1$  “rotates” farther in the full dynamics. This is confirmed by comparing Figs. 8 and 11. On the whole, while it is clear that reinstating all the terms in the dynamics produces quantitative changes, the qualitative behavior—even at this detailed level—is still very similar.

Clearly, the model calculation has simplified the true interstate coupling and neglected  $\omega_{01}$ . However, the insight gained from this model has exciting implications. The potentials  $V_{00}(t)$  and  $V_{01}(t)$  can be parametrized. (In fact, they are often known extremely accurately for the attractive part of the potential.) If the  $V_{00}(t)$  potential is known, then the elastic scattering problem can be solved by standard methods,<sup>32</sup> yielding both  $\theta(b)$  and  $R(t)$  for each impact parameter. The traditional route to inversion of potentials in elastic scattering<sup>33</sup> is to first assume a parametrized  $\theta(b)$ , then to use semiclassical methods to obtain the differential cross section. The classical deflection function is then optimized to give the best fit to the observed DCS. Finally,  $\theta(b)$  is inverted to obtain the potential. Our approach reduces the many-state problem to a series of elastic problems. Inverting Eq. (5) allows one to extract the opacity functions for each  $j$  state, at least for  $\theta$  values beyond the rainbow. The parametrized potentials can then be optimized to obtain the best fit to the experimental data using Eqs. (9a) and (9b). The insight gained from the use of Eqs. (9) can guide the adjustment of the parameters. The advantage of this method for potential inversion is that each coupling element can be adjusted independently of all others. Clearly, the advantage of such a semiclassical framework for inversion is that the coupling

can be optimized at each separate  $\theta$ . A recalculation of the DCS using close coupling methods would require a new global solution of the DCS for each change in the potential. Furthermore, an inspection of the time evolution of the system is intuitively appealing and the contribution of each part of the potential can be readily assessed.

## V. CONCLUSIONS

We have used a semiclassical (classical path) approximation to investigate the quantum dynamics of Ar+HF ( $j=0 \rightarrow j'=0, 1$ ) on the Hutson *H6* potential.<sup>3</sup> We were able to reproduce previous DCS obtained from close-coupled calculations. The time-dependent approach is readily implemented using the semiclassical approximation offering an intuitive appeal which is often more difficult to obtain from the time-independent CC calculations. (Recent work by Alexander<sup>34</sup> has suggested a new representation of time-independent data which could probably furnish most of the mechanistic details described here.) In particular, it is often easier to visualize the influence of the potential on the dynamics when its contributions are localized in time. In an earlier publication,<sup>2</sup> we were only able to analyze whether a given potential feature was important or not by comparing CC calculations in the presence of and in the absence of that feature. For instance, by artificially making the repulsive wall isotropic, it was observed that the dip in the  $0 \rightarrow 1$  DCS disappeared. From this, it could be inferred that the repulsive anisotropy was crucial for the observation of all aspects of the quantum features, but the extent of the competing contributions of the repulsive and attractive anisotropy could not be clearly gauged. In contrast, the time-dependent picture allows us to “see” how the potential affects the dynamics. In particular, plots of the expansion coefficients  $\langle Y_{jm} | \Psi(t) \rangle$  in the complex plane seem to represent a significant step forward in allowing us to determine the exact nature of the contribution of each region of the surface to the scattering dynamics.

Furthermore, for this particular system, it was found that all the qualitative features of the dynamics could be reproduced by considering the dynamics of only two rotor states,  $|0,0\rangle$  and  $|1,0\rangle$ . Thus the effect of the potential could be reduced to that of the coupling matrix elements  $V_{00}$  and  $V_{10}$ . Using this two-state model, we were able to rationalize the features observed in our previous paper.<sup>2</sup> Essentially, the quantum feature seen previously is due to the existence of an impact parameter for which the trajectory experiences an overall balance between the attractive and repulsive parts of the potential, resulting in a net zero action. For this trajectory, the collision is found to be asymptotically elastic, returning all flux to  $j'=0$ . Therefore, at this impact parameter, the  $0 \rightarrow 0$  probability (and consequently the differential cross section) goes through a maximum. Probability conservation, of course, ensures a minimum probability into all other channels—particularly  $0 \rightarrow 1$  at this impact parameter.

This has implications for the “inversion” of a potential surface from experimental scattering data. A clear intuitive grasp of the role played by each part of the potential is a great aid in guiding the adjustment of a parametrized po-

tential in order to improve agreement with experimental input. In particular, it seems that the technique we have explored here shows very distinctively the contrasting effects of attraction and repulsion. While the attractive region of the potential energy surface of van der Waals molecules is often well characterized by potentials derived from spectroscopic data,<sup>3</sup> the repulsive wall is usually much more obscure and often obtained by extrapolation of bound state data.<sup>3,35</sup> However, we envisage being able to employ the techniques explored here to systematically investigate the effect of small changes in the repulsive wall with the goal of improving qualitative agreement with scattering data. Used in conjunction with converged close-coupled results, this could prove a promising approach to obtaining accurate global potential energy surfaces for van der Waals molecules.

## ACKNOWLEDGMENTS

Acknowledgment is made to the Donors of the Petroleum Research administered by the American Chemical Society for support to HRM of this research. Acknowledgement is made to the donors of the Petroleum Research administered by the American Chemical Society for support to MK of this research. We would like to thank Professor Greg Parker (Oklahoma) whose insight into Argand diagrams suggested to us the complex-plane plots of Figs. 7–9. We also thank Les Rawluk (Grande Prairie, Alberta) for carrying out the close coupled calculations.

- <sup>1</sup>L. J. Rawluk, Y. B. Fan, Y. Apelblat, and M. Keil, *J. Chem. Phys.* **94**, 4205 (1991).
- <sup>2</sup>L. J. Rawluk, M. Keil, M. H. Alexander, H. R. Mayne, and J. J. C. Barrett, *Chem. Phys. Lett.* **202**, 291 (1993).
- <sup>3</sup>J. M. Hutson, *J. Chem. Phys.* **96**, 6752 (1992).
- <sup>4</sup>U. Buck, *Comments At. Mol. Phys.* **17**, 143 (1986).
- <sup>5</sup>P. L. Jones, U. Hefter, A. Mattheus, J. Witt, K. Bergmann, W. Müller, W. Meyer, and R. Schinke, *Phys. Rev. B* **26**, 1283 (1982); P. L. Jones, E. Gottwald, U. Hefter, and K. Bergmann, *J. Chem. Phys.* **78**, 3838 (1983), and references therein.
- <sup>6</sup>R. Schinke and J. M. Bowman, in *Molecular Collision Dynamics*, edited by J. M. Bowman (Springer, Berlin, 1982), Chap. 4.
- <sup>7</sup>P. F. Vohralik, R. E. Miller, and R. O. Watts, *J. Chem. Phys.* **90**, 2182 (1989).

- <sup>8</sup>G. A. Parker and R. T. Pack, *J. Chem. Phys.* **68**, 1585 (1978).
- <sup>9</sup>J. J. C. Barrett, H. R. Mayne, M. Keil, and L. J. Rawluk, *Can. J. Chem.* (to be published).
- <sup>10</sup>Hibridon is a package of programs for the time-independent quantum treatment of inelastic collisions and photodissociation written by M. H. Alexander, D. E. Manolopoulos, H.-J. Werner, and B. Follmeg, with contributions by P. F. Vohralik, D. Lemoine, G. Corey, B. Johnson, T. Orlikowski, W. Kearney, A. Berning, A. Degli-Esposti, C. Rist, and P. Dagdigian.
- <sup>11</sup>L. Beneventi, P. Casavecchia, F. Vecchiocattivi, G. G. Volpi, D. Lemoine, and M. H. Alexander, *J. Chem. Phys.* **89**, 3505 (1988).
- <sup>12</sup>R. B. Gerber and R. Alimi, *Isr. J. Chem.* **31**, 383 (1991).
- <sup>13</sup>P. A. M. Dirac, *The Principles of Quantum Mechanics* (Oxford University, Oxford, 1947), pp. 113–125.
- <sup>14</sup>N. F. Mott, *Proc. Cambridge Philos. Soc. Math. Phys. Sci.* **27**, 553 (1931).
- <sup>15</sup>D. R. Bates, *Atomic and Molecular Processes* (Academic, New York, 1962), Chap. 4.
- <sup>16</sup>G. D. Billing, *Comp. Phys. Rep.* **1**, 237 (1984); W. R. Gentry, *Atom-Molecule Collision Theory*, edited by R. B. Bernstein, (Plenum, New York, 1979), pp. 397–401; A. S. Dickinson, *Comp. Phys. Commun.* **17**, 51 (1979), and references therein.
- <sup>17</sup>W. H. Miller and S. Shi, *J. Chem. Phys.* **75**, 2258 (1981).
- <sup>18</sup>W. H. Miller, *Adv. Chem. Phys.* **25**, 69 (1974).
- <sup>19</sup>R. A. Marcus, *Chem. Phys. Lett.* **7**, 525 (1970); *J. Chem. Phys.* **59**, 5135 (1973).
- <sup>20</sup>B. B. Grayce, R. T. Skodje, and J. M. Hutson, *J. Chem. Phys.* **98**, 3929 (1993).
- <sup>21</sup>B. Jackson, *J. Phys. Chem.* **93**, 7699 (1989).
- <sup>22</sup>A. García-Vela and R. B. Gerber, *J. Chem. Phys.* **97**, 3297 (1992).
- <sup>23</sup>R. Schinke, H. Krüger, V. Hermann, H. Schmidt, and F. Linder, *J. Chem. Phys.* **67**, 1187 (1977); C. F. Geise and W. R. Gentry, *Phys. Rev. A* **10**, 2156 (1974).
- <sup>24</sup>L. J. Kovalenko, S. R. Leone, and J. B. Delos, *J. Chem. Phys.* **91**, 6948 (1989).
- <sup>25</sup>R. D. Levine and R. B. Bernstein, *Molecular Reaction Dynamics and Chemical Reactivity* (Oxford University, New York, 1987), p. 861.
- <sup>26</sup>M. S. Child, *Molecular Collision Theory* (Academic, London, 1974), pp. 143–144.
- <sup>27</sup>M. V. Berry and K. E. Mount, *Rep. Prog. Phys.* **35**, 315 (1972).
- <sup>28</sup>K. Haug and H. Metiu, *J. Chem. Phys.* **97**, 4781 (1992).
- <sup>29</sup>M. Karplus, R. N. Porter, and R. D. Sharma, *J. Chem. Phys.* **43**, 3259 (1965).
- <sup>30</sup>Reference 26, pp. 66–67.
- <sup>31</sup>H. R. Mayne and M. Keil, *J. Phys. Chem.* **88**, 883 (1984).
- <sup>32</sup>Reference 25, pp. 141–148.
- <sup>33</sup>U. Buck, *Adv. Chem. Phys.* **30**, 313 (1975); *Rev. Mod. Phys.* **46**, 369 (1974).
- <sup>34</sup>M. H. Alexander, *J. Chem. Phys.* **95**, 8931 (1991); **96**, 6672 (1992).
- <sup>35</sup>D. J. Nesbitt, M. S. Child, and D. C. Clary, *J. Chem. Phys.* **90**, 4855 (1989).